Biosensors and Bioelectronics 142 (2019) 111551

Contents lists available at ScienceDirect

Biosensors and Bioelectronics

journal homepage: www.elsevier.com/locate/bios

A ternary quenching electrochemiluminescence insulin immunosensor based on Mn^{2+} released from MnO_2@Carbon core-shell nanospheres with ascorbic acid quenching AuPdPt–MoS_2@TiO_2 enhanced luminol

Xiaojian Li, Xu Sun, Dawei Fan, Tao Yan, Rui Feng, Huan Wang, Dan Wu, Qin Wei*

Key Laboratory of Interfacial Reaction & Sensing Analysis in Universities of Shandong, School of Chemistry and Chemical Engineering, University of Jinan, Jinan, 250022, China

ARTICLE INFO

Keywords:
Luminol
Electrochemiluminescence resonance energy transfer
Mn^{2+}
Consumed superoxide radical
Insulin

ABSTRACT

This work reported a ternary quenching strategy based on electrochemiluminescence resonance energy transfer (ECL-RET) between luminol/H_2O_2 system and MnO_2 capped carbon nanospheres (MnO_2@C) and Mn^{2+} released from the reduction of MnO_2 and ascorbic acid (AA) consumed superoxide radical ($O_2^{\bullet -}$) for detection of insulin. To improve the ECL behavior of luminol, AuPdPt hybrid nanoparticles decorated MoS_2 nanosheet-coated TiO_2 nanobelt (AuPdPt–MoS_2@TiO_2) were applied to combine with luminol and primary antibodies via covalent linkage which exhibited perfectly catalysis for the electroreduction of H_2O_2. In order to sensitively detect insulin, labels MnO_2@C were used to anchor secondary antibodies via electrostatic interaction and inhibit the ECL intensity of luminol. The perfect overlap of the ECL spectrum of luminol with the absorption spectrum of MnO_2 allowed the ECL-RET to decrease ECL signals of luminol. Specifically, AA was introduced not only to inhibit the ECL of luminol, but also to reduce MnO_2 producing Mn^{2+} which can be reacted with $O_2^{\bullet -}$ to further quench the ECL reaction between luminol and H_2O_2. On the basis of the dual quenching effect of luminol, the sandwich immunosensor was prepared to determine insulin with wide linear range from 0.5 pg mL^{-1} to 60 ng mL^{-1} and a low detection limit of 0.13 pg mL^{-1} (S/N = 3).

1. Introduction

Luminol has been known as an electrochemiluminescence (ECL) luminophore with excellent luminous efficiency, and its ECL behavior has been studied extensively (Dong et al., 2016; Zhu et al., 2017). Reactive oxygen species (ROSs) have been becoming essential species in the enhancement of ECL behavior of luminol, generally including peroxides, superoxide radicals, hydroxyl radicals and singlet oxygen (Haghighi et al., 2015; Jiang et al., 2015). Superoxide radical ($O_2^{\bullet -}$) which is produced by H_2O_2 and dissolved oxygen at positive potential could react with luminol producing excited-state luminol for generating ECL signals (Jiang et al., 2017). Moreover, when immobilizing luminol on the electrode surface, both luminous efficiency and the quantity of luminescent reagent could be improved. During the ECL reaction between luminophores and coreactant, the surface area of the electrode and the rate of electron injection from the electrode interface to the electrolyte solution can be improved by nanomaterials which can further increase the ECL signals (Liang et al., 2014).

The latest research has reported that MoS_2 nanomaterials are an ideal candidate for catalyzing the decomposition of H_2O_2 (Dou et al., 2018; Li et al., 2018), which is attributed to the increasement of electron-electron correlations assisting the planar electric transportation properties (Subbaiah et al., 2016; Wang et al., 2013). TiO_2 has gained much attention due to its large surface area, high surface adsorption, good stability and biocompatibility (Mao et al., 2010). Herein, MoS_2 nanosheet-coated TiO_2 nanobelt (MoS_2@TiO_2) heterostructures with 3D hierarchical configuration were synthesized by a simple hydrothermal method (Zhou et al., 2013). Moreover, S atom of MoS_2 nanosheet surface provide lots of vacant orbitals to immobilize noble metal atoms through coordinate bonds which can further enhance the electroreduction of H_2O_2 (Ma et al., 2016a; Xiangjun et al., 2016). According to our knowledge, both bimetallic and trimetallic nanoparticles have exhibited more excellent catalytic performances than the relevant single nanoparticles (Naveen et al., 2016; Zhang et al., 2014). Besides, noble metal nanoparticles can anchor luminol through covalent linkage between noble metal nanoparticles and the amino-of luminol (Li et al. 2017, 2019). Based on this finding, AuPdPt hybrid nanoparticles decorated MoS_2 nanosheet-coated TiO_2 nanobelt

---

* Corresponding author.
E-mail address: sdjndxwq@163.com (Q. Wei).

https://doi.org/10.1016/j.bios.2019.111551
Received 4 June 2019; Received in revised form 29 July 2019; Accepted 29 July 2019

(AuPdPt–MoS_2@TiO_2) which has perfect catalytic effect on electrochemical reduction of H_2O_2 can be applied to immobilize luminol as the ECL immunosensor's substrate materials.

Recently, two-dimensional (2D)-layered nanosheets and their biological applications have been widely investigated due to their unique characteristics (Fan et al., 2016; Xiong et al., 2017). Manganese dioxide (MnO_2) nanomaterials have been extensively studied due to its rich electrical and catalytic properties (Jikang et al., 2005; Reddy et al., 2009). MnO_2 can be in situ immobilized on carbon spheres surfaces via a simple redox reaction between $KMnO_4$ and carbon (Yong et al., 2014). It's worth noting that Gao et al. reported that Mn^{2+} exhibited the ROS scavenging property which could inhibit the ECL behavior of lucigenin (Gao et al., 2016). MnO_2 with strong reducibility could be fast reduced by ascorbic acid (AA) and glutathione, which makes MnO_2 covert into Mn^{2+} ions (Liu et al., 2018a; Shi et al., 2018). Inspired by the preceding works, MnO_2@Carbon core-shell nanospheres (MnO_2@C) are used as secondary labels to quench the ECL behavior of luminol with the existence of AA in substrate solution.

As we all know, insulin is a peptide hormone which can regulate the metabolism of fats and carbohydrates (Ma et al., 2016b; Xiong et al., 2015). The detection of insulin is particularly meaningful in the application of clinical, because the content of insulin is the most vital indicator of the endocrinal function of beta cells and provides useful basis for the detection of diabetes mellitus, insulinoma, insulin resistant syndrome, etc. (Ying et al., 2011). Thereby, insulin was used as detecting target in this work. Herein, primary antibodies (Ab_1) were anchored on Lu-AuPdPt-MoS_2@TiO_2 through noble metal nanoparticles adsorbing proteins. After secondary antibodies (Ab_2) labeled on MnO_2@Carbon specifically recognized by antigens, the ECL behavior of luminol decreased obviously in the presence of coreactant H_2O_2 and AA. The possible quenching mechanism was studied and we found that not only Mn^{2+} which was released from MnO_2 consumed $O_2^{\bullet-}$ to inhibit the ECL reaction between luminol and H_2O_2, but also the perfect overlap of the ECL spectrum of luminol with the absorption spectrum of MnO_2 allowed the ECL-RET to decrease ECL signals of luminol.

2. Experimental section

2.1. Preparation of MoS_2@TiO_2

TiO_2 nanobelt was prepared and the detailed process was shown in Supplementary Material. Then, MoS_2@TiO_2 heterostructures were prepared briefly according to published work with slight modifications (Zhou et al., 2013). 25 mg $Na_2MoO_4 \cdot 2H_2O$ and 60 mg thioacetamide were dissolved in 40 mL ultrapure water. Following by, 20 mg TiO_2 nanobelt was added in the above solution under ultrasound 1 h. The mixed solution was transferred to 100 mL Teflon-lined stainless-steel autoclave and heated at 240 °C for 24 h. When the solution was naturally cooled to room temperature, MoS_2@TiO_2 heterostructures was centrifuged and washed several times with ultrapure water and ethanol, and then was dried in vacuum at 60 °C for 12 h.

2.2. Preparation of Lu-AuPdPt-MoS_2@TiO_2

1 mL 2.5 mg mL^{-1} MoS_2@TiO_2 was put in the solution contained 4.3 mg Pluronic F127 and 0.35 mg hexadecylpyridinium chloride monohydrate under stirring. Then, 30 μL 1% $HAuCl_4$, 0.0035 g Na_2PdCl_4 and 0.00621 g K_2PtCl_4 were added successively in the above solution with stirring 30 min. Finally, 450 μL of 30 mM AA was added dropwise to reduce the mixture solution. After stirring for 1 h, the mixed solution was collected by centrifuging and meanwhile washed with ultrapure water to obtain AuPdPt–MoS_2@TiO_2.

AuPdPt–MoS_2@TiO_2 was redispersed in 5 mL ultrapure water and 1 mL 5 mM luminol was mixed under oscillating 12 h. Luminol was combined with AuPdPt–MoS_2@TiO_2 via covalent linkage between noble-metal nanoparticles and the amino-of luminol, centrifuging to remove dissociative luminol. Finally, the nanomaterials were vacuum dried at 35 °C. The obtained Lu-AuPdPt-MoS_2@TiO_2 nanomaterials were dispersed in 0.5% chitosan for further use.

2.3. Synthetization of Ab_2-MnO_2@C

Firstly, carbon nanosphere was prepared as follows. 3.47 g glucose was dissolved in 35 mL ultrapure water and transferred to Teflon-lined stainless-steel autoclave and reacted at 180 °C for 5 h. The black solution was centrifuged and washed with ultrapure water until supernatant liquid becoming colorless and transparent. Then, the obtained product was annealed at 500 °C for 5 h. Secondly, 50 mg carbon nanosphere, 0.03 g $KMnO_4$ and 1 mL PDDA were added in 100 mL ultrapure water under ultrasound 1 h and refluxed at 180 °C for 25 min. Then, the round-bottom flask was immediately put into the cooling water until the temperature cooling down, centrifuging and washing with ultrapure water. The obtained product was annealed at 180 °C for 5 h.

MnO_2@C and insulin secondary antibodies were conjugated using an electrostatic effect. In detail, 2 mg MnO_2@C was added in 1 mL PBS (pH 7.4) with ultrasound 1 h. Then 500 μL 500 μg mL^{-1} Ab_2 was mixed with the above solution with stirring 6 h at 4 °C. Finally, the above solution was mixed with 100 μL 1% BSA which can confine the non-specific sites, and washed with ultrapure water to remove unbound BSA by centrifuging. The resulting Ab_2-MnO_2@C was dispersed in PBS (pH 7.4) prior to use.

2.4. Immunoassay development for detecting insulin

Scheme 1 displayed the fabricated process of immunosensor. Before dropping nanomaterials and biomolecules, ITO was sliced into $1 \times 1.5\ cm^2$ sections and washed with acetone, ethanol, and ultrapure water each for 1 h under ultrasonication, then dried by nitrogen prior to use. Subsequently, 5 μL 10 mg mL^{-1} Lu-AuPdPt-MoS_2@TiO_2 were modified on the ITO surface. Afterward, 5 μL Ab_1 (500 μg mL^{-1}) was incubated with the modified electrode surface at 4 °C for at least 2 h. The modified-ITO was rinsed completely using ultrapure water, following by 3 μL 1 wt% BSA solution was incubated with the modified-ITO surface to block nonspecific sites for 1 h at 4 °C. After rinsed with ultrapure water, 6 μL different concentrations of insulin solutions were incubated at 4 °C for 1.5 h. At last, Ab_2-MnO_2@C solution was combined with Insulin/BSA/Ab_1/Luminol-AuPdPt-MoS_2@TiO_2 modified ITO through immunoreaction between antibodies and antigens. The resulting immunosensor (Ab_2-MnO_2@C/Insulin/BSA/Ab_1/Luminol-AuPdPt-MoS_2@TiO_2/ITO) was reserved at 4 °C for further use.

2.5. The detecting conditions of ECL measurement

The substrate solution in ECL cell contained 10 mL PBS (pH 8.5) with 8 mM H_2O_2. The scan rate was set at 0.15 V s^{-1}. The working potential was 0–1.0 V and the photomultiplier tube was set at 800 V. Subsequently, the fabricated immunosensor was put in the cell and investigated the ECL performance.

3. Results and discussion

$$H_2O_2 \underset{AuPdPt-MoS_2@TiO_2}{\overset{-e^-}{\rightarrow}} O_2^{-\bullet} + H_2O \tag{1}$$

$$Lu - H \underset{H^+}{\overset{OH^-}{\rightleftharpoons}} Lu^- \overset{-e^-}{\rightarrow} Lu^{-\bullet} \tag{2}$$

$$Lu^{-\bullet} + O_2^{-\bullet} \rightarrow 3 - AP^{2-*} + N_2 \tag{3}$$

$$O_2^{-\bullet} + Lu^- \rightarrow Lu^{-\bullet} + HO_2^- \tag{4}$$

$$3 - AP^{2-*} \rightarrow 3 - AP^{2-} + hv \tag{5}$$

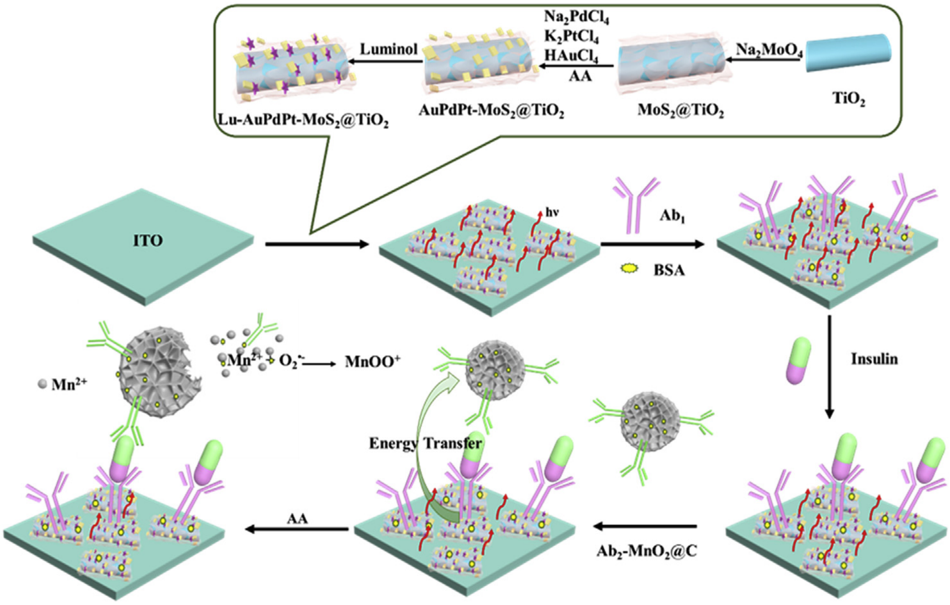

Scheme 1. The preparation process of the developed ECL immunosensor.

$$MnO_2 + AA + H^+ \rightarrow Mn^{2+} + DHAA + H_2O \tag{6}$$

$$Mn^{2+} + O_2^{-\bullet} \rightarrow MnOO^+ \tag{7}$$

3.1. Materials characterization

Fig. 1A and B shows the SEM imagines of TiO_2 nanobelt and $MoS_2@TiO_2$. The wide of TiO_2 nanobelt was distributed in the range of 20 nm–300 nm and the surface of TiO_2 nanobelt became rough through acid treatment which can offer many energy nucleation sites for nucleating and growing MoS_2 nanosheets. As illustrated in Fig. 1B, the thin MoS_2 nanosheets are uniformly wrapped on TiO_2 nanobelts surface. To investigate the crystal structure, XRD was used to characterize pure TiO_2, pure MoS_2 and $MoS_2@TiO_2$ heterostructures. The diffraction peaks of pure MoS_2 corresponded to the standard peaks of hexagonal phase MoS_2 (JCPDS No. 37-1492) and diffraction peaks were observed at 13.3° (002), 32.7° (100), 39.5° (103), and 60.1° (008) with cell parameters a:3.161 Å, b:3.161 Å and c:12.299 Å (curve a in Fig. S1A). As depicted in Fig. S1A curve b, the peaks of the pure TiO_2 were assigned to (101), (004), (200), (105), (211), (204), and (116) which matched the standard peaks of anatase phase TiO_2 (JCPDS card no. 21-1272). In the XRD pattern of $MoS_2@TiO_2$ heterostructures, all the diffraction peaks were consistent with the pure MoS_2 and TiO_2 (curve c in Fig. S1A). Fig. 1C showed the morphology of AuPdPt–$MoS_2@TiO_2$ which demonstrated that Au, Pd and Pt nanoparticles were immobilized on $MoS_2@TiO_2$ heterostructures surface through noble metal-S chemical bond. Moreover, the energy dispersive X-Ray spectroscopy (EDX) of AuPdPt–$MoS_2@TiO_2$ was displayed in Fig. 2A which indicated the main elements of $MoS_2@TiO_2$ heterostructures including Au, Pd, Pt, Mo, S, O and Ti. Besides, X-ray photoelectron spectroscopy (XPS) was utilized to determinate elemental composition and valence states of AuPdPt–$MoS_2@TiO_2$. XPS survey spectrum contained Au 4f, Pd 3d, Pt 4f, Mo 3d, S 2p, Ti 2p and O 1s peaks (Fig. 2B). The fitted peaks of Au 4f located at 83.1 and 86.5 eV were attributed to Au $4f_{7/2}$ and Au $4f_{5/2}$,

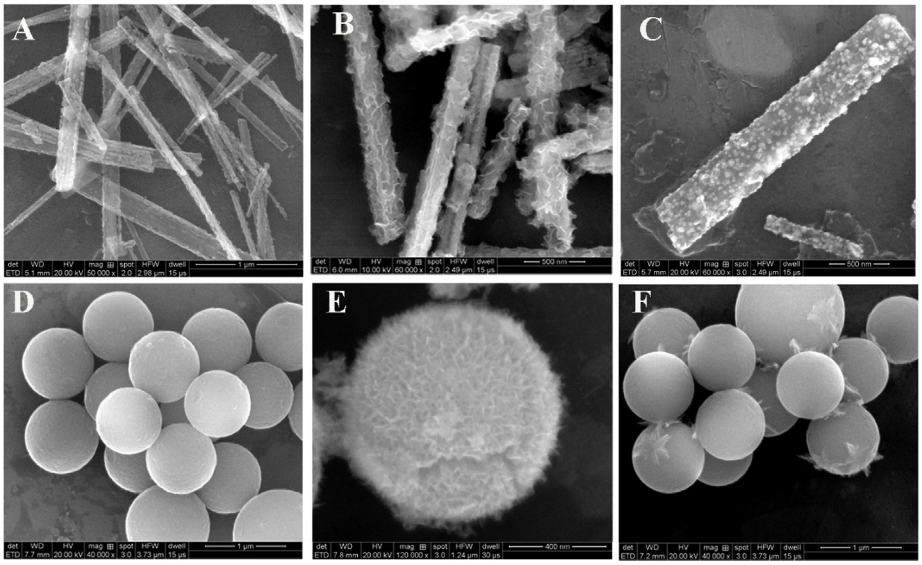

Fig. 1. The SEM imagines of TiO_2 nanobelt (A), $MoS_2@TiO_2$ (B), AuPdPt–$MoS_2@TiO_2$ (C), carbon nanospheres (D), $MnO_2@C$ (E) and $MnO_2@C$ with treatment of AA (F).

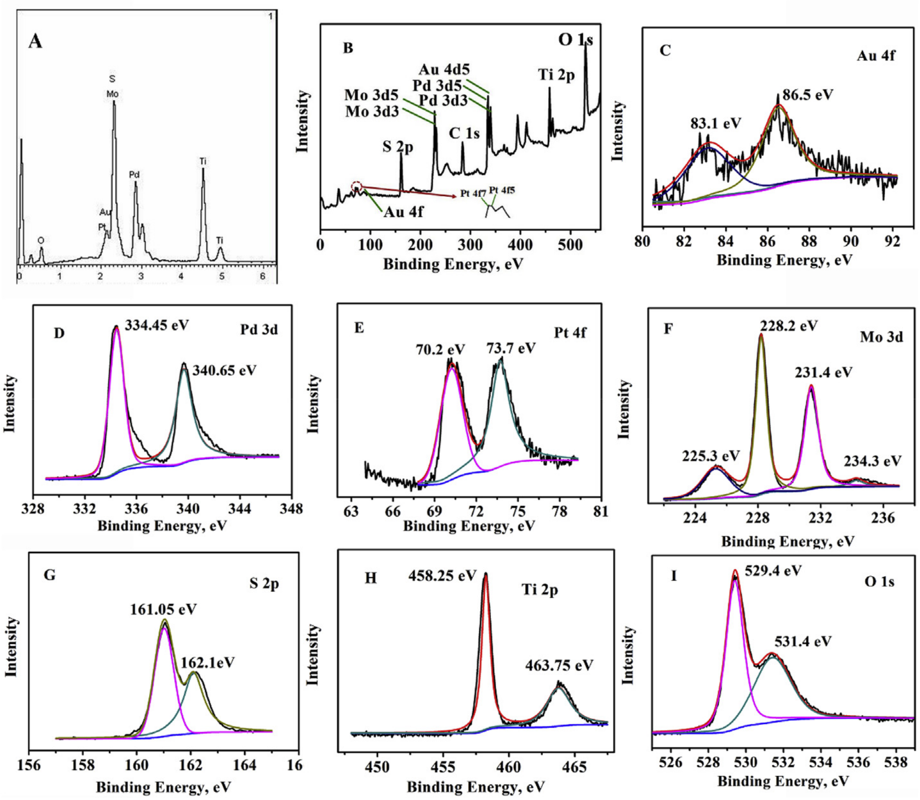

Fig. 2. EDX of AuPdPt–MoS_2@TiO_2 (A); XPS survey spectrum (B); XPS high resolution spectra of Au 4f (C), Pd 3d (D), Pt 4f (E), Mo 3d (F), S 2p (G), Ti 2p (H) and O 1s (I).

which indicated that the formation of metallic gold (Fig. 2C) (Dong et al., 2015). As illustrated in the high-resolution spectra of Pd 3d (Fig. 2D), the fitted peaks at 334.45 eV and 340.65 eV were assigned to metallic Pd (Wang et al.). Fig. 2E was the high-resolution spectra of Pt 4f with binding energies of 70.2 eV and 73.7 eV, indicating the existing of metallic Pt (Céline et al., 2008). Fig. 2F and G were the XPS spectra of Mo 3d and S 2s and represented that the binding energies of Mo $3d_{5/2}$, Mo $3d_{3/2}$, S $2p_{3/2}$ and S $2p_{1/2}$ peaks were respectively situated at 228.2 eV, 231.4 eV, 161.05 eV and 162.1 eV, indicating that Mo^{4+} existed in MoS_2@TiO_2 heterostructures (Qiao et al., 2017). In addition, the fitted peaks at 225.3 eV and 234.3 eV were assigned to S 2s and Mo^{6+} 3d in Fig. 2F, separately (Xin et al., 2018). As shown in Fig. 2H, two peaks at 458.25 and 4643.75 eV belonged to Ti^{4+} $2p_{3/2}$ and Ti^{4+} $2p_{1/2}$ peaks. In the O 1s XPS spectra, the fitted peaks which located at 529.4 eV and 531.4 eV were mainly attributed to Ti–O (Lee and Park, 2019). Both EDX and XPS of AuPdPt–MoS_2@TiO_2 indicated noble metal particles were successfully anchored on the surface of MoS_2@TiO_2 heterostructures.

The hybrid MnO_2@C nanospheres were prepared by a two-step hydrothermal method. After carbon nanospheres synthesized, MnO_2 shells were in situ grown on the carbon nanospheres surfaces. Fig. 1D represented the SEM image of carbon nanospheres with the mean diameter about 500 nm. After MnO_2 shells grown on the carbon nanospheres surface, the morphology of MnO_2@C was flower-like (Fig. 1E). The XRD pattern of carbon nanospheres was performed and two peaks at about 22.2° and 42.8° were belonged to the (002) and (101) planes of graphite (Fig. S1B curve a). Moreover, as illustrated in the XRD pattern of MnO_2@C (Fig. S1B curve b), the whole diffraction peaks can be consistent with MnO_2 (JCPDS No. 44-0141). Diffraction peaks were observed at 30.3° (310), 37.5° (211), 49.9° (411), 60.3° (521), 65.1° (002) and 69.7° (541). The additional peaks found at 22.2° and 42.8° were attributed to carbon nanospheres. When AA was added in the MnO_2@C solution, the shell MnO_2 was decomposed into Mn^{2+}. As shown in Fig. 1F, only carbon nanosphere and a bit of MnO_2 were remained.

3.2. ECL mechanism of Luminol-AuPdPt-MoS_2@TiO_2/H_2O_2 system and MnO_2@C quenching Luminol-AuPdPt-MoS_2@TiO_2 without AA and with AA

Herein, H_2O_2 was used as coreactant to react with luminophore luminol generating ECL signals. Nanomaterials with hastening the electroreduction of H_2O_2 can enhance the ECL intensity of luminol. In this work, AuPdPt–MoS_2@TiO_2 was applied to construct the immunosensor as substrate material and the catalytic effect was investigated through cyclic voltammetry (CV) in Fig. 3A. Compared with bare ITO (curve a in Fig. 3A), the nonconductivity of TiO_2 made the current intensity decrease (curve b in Fig. 3A), indicating TiO_2 couldn't facilitate the electroreduction of H_2O_2. MoS_2@TiO_2 played a superior effect on the electroreduction of H_2O_2 (curve c in Fig. 3A). While AuPdPt–MoS_2@TiO_2 was immobilized on the ITO surface, the current signals were optimal (curve d in Fig. 3A). Therefore, AuPdPt-–MoS_2@TiO_2 exhibited excellent catalysis effect on the electroreduction of H_2O_2 to generate superoxide anion $O_2^{\bullet -}$ (eq. (1)), when the potential was scanned from 0 to 1.0 V in the positive direction. Then, luminol could deprotonate forming luminol anion (Lu^-) which can generate intermediate oxidation state of luminol ($Lu^{-\bullet}$) under positive scanning (eq. (2)). Subsequently, the reaction of $Lu^{-\bullet}$ and strong oxidant $O_2^{\bullet -}$ could occur to form the excited state of 3-aminophthalate (3-AP^{2-*}) for releasing ECL signals (eq. (3)). Moreover, the strong oxidant $O_2^{\bullet -}$ can also make Lu^- forming $Lu^{-\bullet}$ (eq. (4)). When excited state 3-AP^{2-*} back to ground state 3-AP^{2-}, strong ECL emission was generated (eq. (5)) and the ECL spectra of luminol illustrated that the luminescence was at 435 nm (curve a in Fig. 3B).

After luminol combined with AuPdPt–MoS_2@TiO_2, excellent ECL signals were observed in Fig. S2 (curve a in Fig. S2, Supplementary

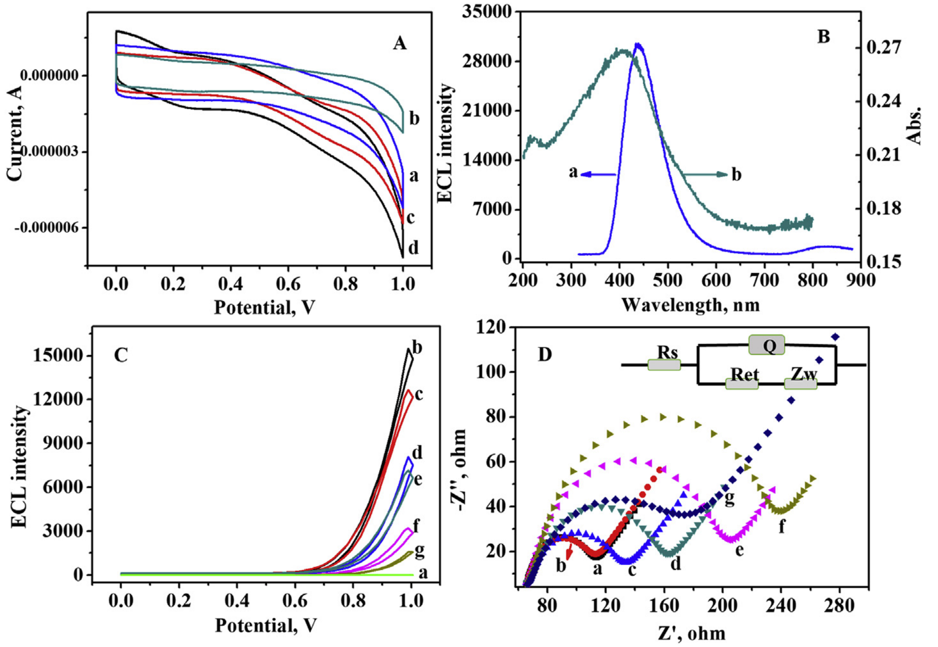

Fig. 3. (A) CV of bare ITO (a), TiO_2/ITO (b), MoS_2@TiO_2/ITO (c) and AuPdPt–MoS_2@TiO_2/ITO (d) performed in PBS (pH = 8.0) containing 10 mM H_2O_2; (B) the ECL emission spectra of luminol (curve a) and the UV–vis absorption spectra of MnO_2@C (curve b); (C) ECL signals obtained on bare ITO (a), Lu-AuPdPt-MoS_2@TiO_2/ITO (b), Ab_1/Lu-AuPdPt-MoS_2@TiO_2/ITO (c), BSA/Ab_1/Lu-AuPdPt-MoS_2@TiO_2/ITO (d), Insulin/BSA/Ab_1/Lu-AuPdPt-MoS_2@TiO_2/ITO (e), Ab_2-MnO_2@C/Insulin/BSA/Ab_1/Lu-AuPdPt-MoS_2@TiO_2/ITO (f), Ab_2-MnO_2@C/Insulin/BSA/Ab_1/Lu-AuPdPt-MoS_2@TiO_2/ITO with AA (g); (D) EIS of bare ITO (a), Lu-AuPdPt-MoS_2@TiO_2/ITO (b), Ab_1/Lu-AuPdPt-MoS_2@TiO_2/ITO (c), BSA/Ab_1/Lu-AuPdPt-MoS_2@TiO_2/ITO (d), Insulin/BSA/Ab_1/Lu-AuPdPt-MoS_2@TiO_2/ITO (e), Ab_2-MnO_2@C/Insulin/BSA/Ab_1/Lu-AuPdPt-MoS_2@TiO_2/ITO (f), Ab_2-MnO_2@C/Insulin/BSA/Ab_1/Lu-AuPdPt-MoS_2@TiO_2/ITO with AA (g) performed in 2.5 mM $Fe(CN)_6^{3-/4-}$ and 0.1 M KNO_3; The inset was the equivalent circuit for EIS.

Material). When 200 µL 100 mM AA was added in the substrate solution containing 8 mM H_2O_2, the ECL intensity of Lu-AuPdPt-MoS_2@TiO_2 decreased to 47.43% (curve b in Fig. S2). AA has been found to be able to inhibit the ECL of luminol greatly due to AA as an antioxidant consuming ROS (Hong et al., 2008). However, when MnO_2@C was cast on the modified electrode surface (Lu-AuPdPt-MoS_2@TiO_2/ITO), the ECL intensity further decreased to 18.95% though without AA (curve c in Fig. S2). To research the quenching mechanism, the ECL emission spectra of luminol (curve a in Fig. 3B) and the UV–vis absorption spectra of MnO_2@C (curve b in Fig. 3B) were depicted. The ECL spectra of luminol exhibited maximum emission at 435 nm and the emission range was from 360 nm to 660 nm. And the absorption range of MnO_2@C was from 250 nm to 670 nm which maximum absorption peak was at 409 nm. Thus, the overlap between the absorption spectra of MnO_2@C and the ECL emission spectra of luminol led to the ECL quenching of luminol through ECL energy transfer. When AA was added in the substrate solution containing 8 mM H_2O_2, the ECL intensity obviously decreased to 4.38% (curve d in Fig. S2) compared with the ECL signals of MnO_2@C/Lu-AuPdPt-MoS_2@TiO_2/ITO without AA. Besides AA consuming ROS and the ECL energy transfer between MnO_2 and luminol, another reason was that AA could reduce MnO_2 forming Mn^{2+} (eq. (6)), then Mn^{2+} could react with $O_2^{\bullet -}$ generating $MnOO^+$ (eq. (7)) (Joshi, 2017; Liu et al., 2018b). As we all know, $O_2^{\bullet -}$ was the essential species to generate ECL emission of luminol. Therefore, the developed ternary-quenching strategy based on the consumption of $O_2^{\bullet -}$ through AA and Mn^{2+} and ECL energy transfer was applied to fabricate ECL immunosensor.

3.3. Characterizations of the developed ECL immunosensor

To estimate the preparation of the proposed immunosensor in different steps, ITO electrode was assembled and characterized by ECL and EIS. Firstly, the bare ITO electrode exhibited no obvious ECL signal (curve a in Fig. 3C), which showed a small semicircle domain (curve a in Fig. 3D) attributed to free electron-transfer process. When Lu-AuPdPt-MoS_2@TiO_2 was cast on the pretreated ITO surface, excellent ECL signal was showed (curve b). Though Au, Pd, Pt and MoS_2 exhibited favorable conductivity, the poor conductivity of chitosan and TiO_2 made the electron transfer resistance of $[Fe(CN)_6]^{3-/4-}$ on Lu-AuPdPt-MoS_2@TiO_2/ITO decrease a little bit (curve b in Fig. 3D). When Ab_1 (curve c), BSA (curve d) and insulin (curve e) were assembled on the modified ITO electrode, the ECL intensity decreased successively, which was ascribed to Ab_1, BSA and insulin as nonconductive biomolecules hindering the electron transfer between luminophores luminol and coreactant H_2O_2. Moreover, the semicircle domains were consecutively raised (curves c, d and e in Fig. 3D) due to proteins inhibiting the electron transfer. As we all know, the labels Ab_2-MnO_2@C were incubated with BSA to block nonspecific sites, thus the ECL signals decreased (curve f) which was ascribed to the proteins preventing and ECL energy transfer. Similarly, the electron transfer resistance value was also increased due to proteins' inhibiting (curve f in Fig. 3D). When AA was added in the substrate solution, the ECL intensity was further decreased (curve g) which was consistent with the above-mentioned hypothesis. Since AA can reduce MnO_2 which can make Ab_2 peeling from labels, the semicircle domains were decreased (curve g in Fig. 3D). Therefore, the ECL results together with EIS results indicated that the ECL immunosensor was successfully constructed as expected.

3.4. Optimization of experimental conditions

As represented in Fig. S3A the effect of coreactant H_2O_2 on the ECL signal of Lu-AuPdPt-MoS_2@TiO_2/ITO was indicated. The ECL intensity increased with increasing the concentration of coreactant H_2O_2 to 8 mM, then changed slightly when the concentration of coreactant H_2O_2 was more than 8 mM. Hence, 8 mM was chosen as the appropriate concentration. And Fig. S3B represented the influence of pH on the ECL performance of luminol and excellent ECL behavior could be shown in alkaline medium. With increasing pH value, the ECL signals obviously increased and when the pH was more than 8.5, ECL intensity reached a plateau. Accordingly, the pH value in this experiment was chosen as 8.5. On the basis of quenching mechanism, the ECL quenching efficiency relied on the quantity of Mn^{2+} generating from the reduction of MnO_2@C via AA. As depicted in Fig. S3C, the ECL intension decreased sharply with raising the concentrations of AA. When AA concentrations was 100 mM, the difference between Insulin/BSA/Ab_1/Lu-AuPdPt-MoS_2@TiO_2/ITO and Ab_2-MnO_2@C/Insulin/BSA/Ab_1/Lu-AuPdPt-MoS_2@TiO_2/ITO reached a platform. Therefore, 100 mM AA was provided optimal conditions for following ECL detecting to insure satisfying sensitivity.

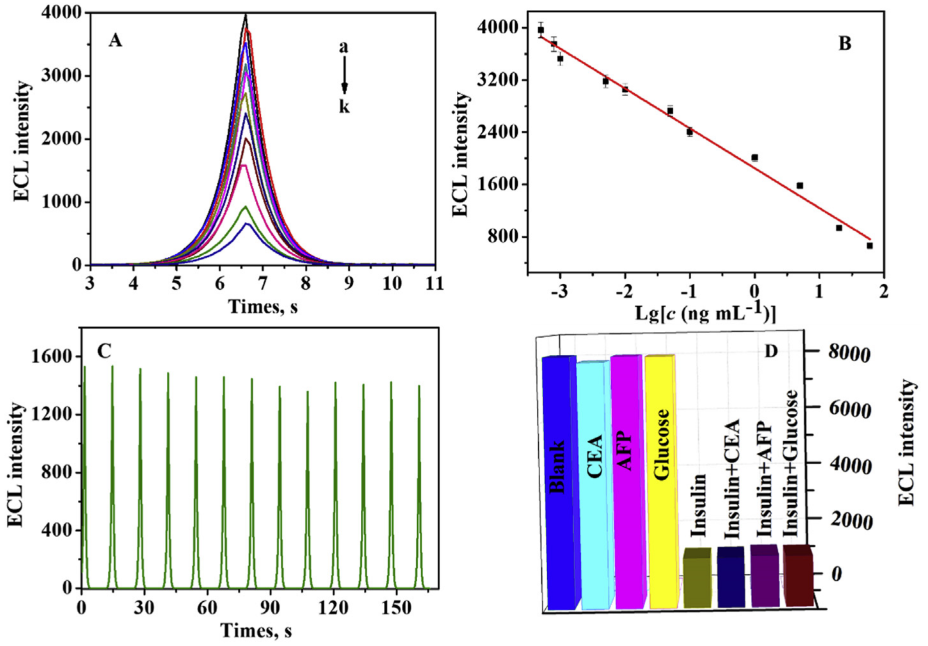

Fig. 4. (A) ECL response of the different concentration of insulin, from a to k: 5E-4, 8E-4, 1E-3, 0.005, 0.01, 0.05, 0.1, 1, 5, 20 and 60 ng mL^{-1}; (B) Calibration curve of the immunosensor; (C) Stability of ECL emissions under continuous scanning for 13 cycles in PBS (pH = 8.5) containing 8 mM H_2O_2 for detection of 5 ng mL^{-1} insulin; (D) Selectivity of the proposed ECL immunosensor against different non-targets: CEA (100 ng mL^{-1}), AFP (100 ng mL^{-1}), glucose (100 ng mL^{-1}), and 5 ng mL^{-1} insulin with 100 ng mL^{-1} interferences. Error bars = RSD ($n = 3$).

3.5. *Detection of insulin with the developed immunosensor*

In order to estimate the sensitivity of our system, the fabricated immunosensor was incubated with different concentrations of insulin and secondary antibodies' labels, based on immunoreaction. Under the optimum conditions, the ECL intension declined accordingly upon rising concentrations of insulin (curve a-k in Fig. 4A). Fig. 4B depicted the relationship between the logarithm of insulin concentrations and ECL intensities in the range from 0.5 pg mL^{-1} to 60 ng mL^{-1}. The linear regression equation was $I = -610.4 \lg c + 1848.3$, and the correlation coefficient and detection limit were 0.9887 and 0.13 pg mL^{-1}, respectively. These results demonstrated that the developed immunosensor was more sensitive than the other existing insulin detecting method (Table S1). This low detection limit could be ascribed to the following factors: (i) AuPdPt–MoS_2@TiO_2 improved the ECL behavior of luminol producing high and stable ECL intensity; the quenching strategy was based on ECL energy transfer between ECL donor luminol and ECL acceptor MnO_2@C (ii) and Mn^{2+} which was generated from the reduction of MnO_2@C by AA, consumed $O_2^{\bullet -}$ forming $MnOO^+$ (iii).

3.6. *Stability, specificity and reproducibility of the insulin immunosensor*

Operation stability is the essential elements to estimate the potential of developed ECL immunosensor in real sample. First, the stability of Lu-AuPdPt-MoS_2@TiO_2 which was cast on ITO surface was detected via consecutive cyclic potential scan for 12 cycles. As shown in Fig. S4, the ECL intension was quite stable and the relative standard deviation (RSD) was 1.31%. When the immunosensor was incubated with 5 ng mL^{-1} insulin, the ECL intensities were determined through consecutive cyclic potential scan for 13 cycles (Fig. 4C) and the RSD was 4.25%. It can be seen that both of the RSD were less than 5%, indicating that the stabilities of the ECL immunosensor were satisfying. In addition, the storage stability of the fabricated ECL immunosensor incubated with 5 ng mL^{-1} insulin was investigated through recording the ECL response after 10-day storage at 4 °C. As shown in Fig. S5, ten days later, the ECL intensity declined 33.2% compared to the primal ECL intension.

To investigate the selectivity and specificity of insulin detection method, the prepared ECL immunosensor was incubated with other interferences (CEA, AFP and glucose) and the results were represented in Fig. 4D. Compared with blank experiment, when detection object only contained interferences, the ECL intensity was no obvious changed. When the immunosensor was hatched with the mixture including 5 ng mL^{-1} of insulin with 100 ng mL^{-1} interferences (CEA, AFP and glucose), the ECL intensity exhibited no obvious effect compared with the ECL intensity of the 5 ng mL^{-1} insulin only. These results indicated that the proposed method exhibited acceptable selectivity, which could be ascribed to the resultful surface blocking by BSA and the highly specific bindings between the antibodies and antigens.

The reproducibility of the proposed immunosensor was acquired through measuring seven same electrodes. The RSD was 2.04% for analyzing 5 ng mL^{-1} insulin (Fig. S6), revealing that the reproducibility of the immunosensor was satisfying.

3.7. *Application of the prepared ECL immunosensor in human serum*

For assessing the feasibility of the ECL immunosensor for insulin detection, the immunosensor was investigated by adding different insulin concentrations and detecting the recovery by standard addition method. Table 1 depicted the recovery of insulin in the range of 94–112%, thereby demonstrating the reliability and practicality of this developed immunosensor.

4. Conclusion

In conclusion, a signal-quenching ECL determination was proposed based on the novel ternary quenching of MnO_2@C with AA towards luminol/H_2O_2 system. The as-synthesized Lu-AuPdPt-MoS_2@TiO_2 was employed to anchor luminol and amplify the ECL behavior of luminol which provided excellent platform for insulin detection. The ternary quenching strategy can be summarized as follows: (i) AA can inhibit the

Table 1
Analytical application of the immunosensor in human serum.

Sample	Addition (ng mL^{-1})	Found (ng mL^{-1})	Recovery (%)
1	60	60.07	100.1
2	15	15.12	100.8
3	5	5.15	103
4	0.1	0.098	98
5	0.05	0.056	112
6	0.0005	0.00047	94

ECL emission of luminol due to AA as an antioxidant consuming ROS; (ii) The ECL emission spectrum of luminol was overlapped suitably with the absorption spectrum of MnO_2@C, which could insure getting high-efficiency ECL-RET; (iii) MnO_2@C was dissolved by the reduction of AA producing Mn^{2+} which reacted with $O_2^{\cdot -}$ consuming the essential species of ECL reaction. The present work would be potentially meaningful for understanding the role of Mn^{2+} in ECL and provide a promising approach to develop efficient immunosensor in clinical application.

Declaration of competing interest

The authors declare that they have no known competing financial interests or personal relationships that could have appeared to influence the work reported in this paper.

CRediT authorship contribution statement

Xiaojian Li: Conceptualization, Data curation, Writing - original draft. **Xu Sun:** Methodology, Writing - review & editing. **Dawei Fan:** Formal analysis. **Tao Yan:** Formal analysis. **Rui Feng:** Methodology, Writing - review & editing. **Huan Wang:** Methodology. **Dan Wu:** Formal analysis. **Qin Wei:** Funding acquisition, Project administration.

Acknowledgements

This study was supported by the National Key Scientific Instrument and Equipment Development Project of China (No.21627809) and National Natural Science Foundation of China (Nos. 21575050 and 21777056).

Appendix A. Supplementary data

Supplementary data to this article can be found online at https://doi.org/10.1016/j.bios.2019.111551.

References

Céline, D., Philippe, L., Claire, M., Jean-Yves, P., Valeri, P., Frédéric, H., Guillaume, V., 2008. Langmuir 24 (11), 5832–5841.
Dong, Y., Gao, T., Zhou, Y., Chu, X., Wang, C., 2015. Spectrochim. Acta Part A Molecular & Biomolecular Spectroscopy 134 (134C), 225–232.
Dong, Y.P., Wang, J., Peng, Y., Zhu, J.J., 2016. J. Electroanal. Chem. 781, 109–113.
Dou, B., Yang, J., Yuan, R., Xiang, Y., 2018. Anal. Chem. 90, 5945–5950.
Fan, H., Yan, G., Zhao, Z., Hu, X., Zhang, W., Liu, H., Fu, X., Fu, T., Zhang, X.B., Tan, W., 2016. Angew Chem. Int. Ed. Engl. 55 (18) 5611-5611.
Gao, W., Liu, Z., Qi, L., Lai, J., Kitte, S.A., Xu, G., 2016. Anal. Chem. 88 (15), 7654.
Haghighi, B., Tavakoli, A., Bozorgzadeh, S., 2015. Electrochim. Acta 154, 259–265.
Hong, D., Wu, X., Wang, Y., Zhou, W., Chen, G., 2008. Electrochim. Acta 53 (16), 5113–5117.
Jiang, X., Wang, H., Yuan, R., Chai, Y., 2015. Biosens. Bioelectron. 63, 33–38.
Jiang, X., Wang, Z., Wang, H., Zhuo, Y., Yuan, R., Chai, Y., 2017. Chem. Commun. 9705–9708.
Jikang, Y., Wei-Na, L., Sinue, G., Suib, S.L., 2005. J. Am. Chem. Soc. 127 (41), 14184–14185.
Joshi, R., 2017. Radiat. Phys. Chem. 139, 74–82.
Lee, M.K., Park, Y.C., 2019. Langmuir 35 (6), 2066–2077.
Li, F., Feng, J., Gao, Z., Shi, L., Wu, D., Du, B., Wei, Q., 2019. ACS Applied Materials & Interfaces11. pp. 8945–8953.
Li, M., Wang, P., Li, F., Chu, Q., Li, Y., Dong, Y., 2017. Biosens. Bioelectron. 87, 752–759.
Li, S., Liu, Z., Li, J., Chen, A., Chai, Y., Yuan, R., Ying, Z., 2018. ACS Appl. Mater. Interfaces 10 (17), 14483–14490.
Liang, M., Peng, T., Yifeng, T.U., 2014. Electrochem. Commun. 46 (9), 107–110.
Liu, Z., Xianyu, Y., Zheng, W., Zhang, J., Luo, Y., Chen, Y., Dong, M., Wu, J., Jiang, X., 2018a. Anal. Chem. 90 (4), 2765–2771.
Liu, Z., Xianyu, Y., Zheng, W., Zhang, J., Luo, Y., Chen, Y., Dong, M., Wu, J., Jiang, X., 2018b. Anal. Chem. 90 (4), 2765–2771.
Ma, D., Ju, W., Li, T., Zhang, X., He, C., Ma, B., Lu, Z., Yang, Z., 2016a. Appl. Surf. Sci. 383, 98–105.
Ma, H., Li, X., Yan, T., Li, Y., Liu, H., Zhang, Y., Wu, D., Du, B., Wei, Q., 2016b. ACS Appl. Mater. Interfaces (16), 10121–10127.
Mao, L.I., Yuan, R., Chai, Y., Ying, Z., Xia, Y., 2010. Sens. Actuators B Chem. 149 (1), 226–232.
Naveen, M.H., Gurudatt, N.G., Noh, H.B., Shim, Y.B., 2016. Adv. Funct. Mater. 26 (10), 1590–1601.
Qiao, S., Zhang, B., Feng, K., Cong, R., Yu, W., Fu, G., Wang, S., 2017. ACS Appl. Mater. Interfaces 9 (21), 18377–18387.
Reddy, A.L., Shaijumon, M.M., Gowda, S.R., Ajayan, P.M., 2009. Nano Lett. 9 (3), 1002.
Shi, W., Song, B., Shi, W., Qin, X., Liu, Z., Tan, M., Wang, L., Song, F., Yuan, J., 2018. ACS Appl. Mater. Interfaces 10 (33), 27681–27691.
Subbaiah, Y.P.V., Saji, K.J., Tiwari, A., 2016. Adv. Funct. Mater. 26 (13), 2046–2069.
Wang, H.M., Wang, C.C., Wang, A.J., Zhang, L., Luo, X., Yuan, P.X., Feng, J.J., 2019;al.,. Sens. Actuators B Chem. 281, 588–594.
Wang, T., Zhu, H., Zhuo, J., Zhu, Z., Papakonstantinou, P., Lubarsky, G., Lin, J., Li, M., 2013. Anal. Chem. 85 (21), 10289–10295.
Xiangjun, Gang, Zhang, Zhang, Yong-Wei, 2016. Nano Res. 9 (8), 2372–2383.
Xin, W.L., Jiang, L.F., Zong, L.P., Zeng, H.B., Shu, G.F., Marks, R., Zhang, X.J., Shan, D., 2018. Sens. Actuators B Chem. 273, 566–573.
Xiong, M., Rong, Q., Meng, H.M., Zhang, X.B., 2017. Biosens. Bioelectron. 89 (Pt 1), 212–223.
Xiong, Y., Deng, C., Zhang, X., Yang, P., 2015. ACS Appl. Mater. Interfaces 7 (16), 8451.
Ying, P., Zhi, Z., Da, H., Huixia, L., Jun, L., Jie, L., Kejing, Z., Weihong, T., 2011. Analyst 136 (20), 4138–4140.
Yong, Z., Meng, Y., Peng, J., 2014. J. Power Sources 259 (7), 219–226.
Zhang, P., Li, R., Huang, Y., Chen, Q., 2014. ACS Appl. Mater. Interfaces 6 (4), 2671–2678.
Zhou, W., Yin, Z., Du, Y., Huang, X., Zeng, Z., Fan, Z., Liu, H., Wang, J., Zhang, H., 2013. Small 9 (1), 140–147.
Zhu, X., Zhai, Q., Gu, W., Li, J., Wang, E., 2017. Anal. Chem. 89, 12108–12114.